

Bulk magnetic properties of distorted square lattice compounds

M^I - Ln TaO₄ ($Ln = \text{Tb, Dy, Ho, Er}$)

Nicola D. Kelly,^{1,*} Ivan da Silva,² and Siân E. Dutton^{1,†}

¹*Cavendish Laboratory, University of Cambridge,*

J J Thomson Avenue, Cambridge, CB3 0HE, United Kingdom

²*ISIS Neutron and Muon Source, Rutherford Appleton Laboratory,*

Didcot, OX11 0QX, United Kingdom

(Dated: March 11, 2026)

Abstract

We report bulk magnetic properties of the monoclinic lanthanide tantalates, $M'-LnTaO_4$ ($Ln = \text{Tb, Dy, Ho, Er}$), where the magnetic Ln^{3+} ions are arranged on a distorted 2D square lattice. The heavier analogue $M'-YbTaO_4$ has been investigated as a spin-orbit-coupled, quasi-two-dimensional frustrated magnet, and the properties of the other $M'-LnTaO_4$ are expected to vary depending on the electronic configuration of the Ln ion, namely Kramers vs non-Kramers behaviour and different crystal electric field parameters. In this work, powder neutron diffraction is used to confirm the crystal structure for $Ln = \text{Tb, Ho, Er}$, and to determine the magnetic structure of $M'-TbTaO_4$, which displays long-range antiferromagnetic (AFM) order below $T_N = 2.1$ K. The Tb^{3+} moments are aligned primarily along the c -axis with AFM nearest-neighbour interactions. Susceptibility data suggest that $M'-DyTaO_4$ may display short-range ordering around 2.7 K, while $M'-HoTaO_4$ and $M'-ErTaO_4$ show AFM correlations but do not order above 1.8 K. Measurements of the magnetic specific heat provide evidence for a Kramers doublet ground states in $M'-ErTaO_4$, similar to its heavier analogue $M'-YbTaO_4$.

I. INTRODUCTION

The spin- $\frac{1}{2}$ Heisenberg square lattice is an important model for frustrated magnetism studies. The two relevant interactions are the nearest-neighbour coupling J_1 , along the sides of the squares, and next-nearest-neighbour J_2 , along the diagonals of the squares. Depending on the relative signs and magnitudes of J_1 and J_2 , three types of classical long-range order (LRO) can be observed (ferromagnetic (FM), columnar antiferromagnetic (AFM), and Néel AFM), and there are also two boundary regions where spin-liquid behaviour is predicted [1–3]. These arise from the competition between J_1 and J_2 when J_2/J_1 is close to ± 0.5 . Several experimental realisations of the Heisenberg square lattice have been studied recently, including $YbBi_2IO_4$ and $YbBi_2ClO_4$ [4], $SrLaCuSbO_6$ and $SrLaCuNbO_6$ [5], and $\alpha\text{-KTi}(\text{C}_2\text{O}_4)_2 \cdot x\text{H}_2\text{O}$ [6], which all order antiferromagnetically at low temperatures. However, a small number of materials have been found to resist order and are therefore considered candidates for the spin-liquid behaviour predicted at $J_2/J_1 \approx \pm \frac{1}{2}$, including transition-metal

* ne281@cam.ac.uk

† sed33@cam.ac.uk

oxides $\text{Sr}_2\text{Cu}(\text{Te}_{1-x}\text{W}_x)\text{O}_6$ [7, 8] and a rare-earth oxide NdKNaNbO_5 [9].

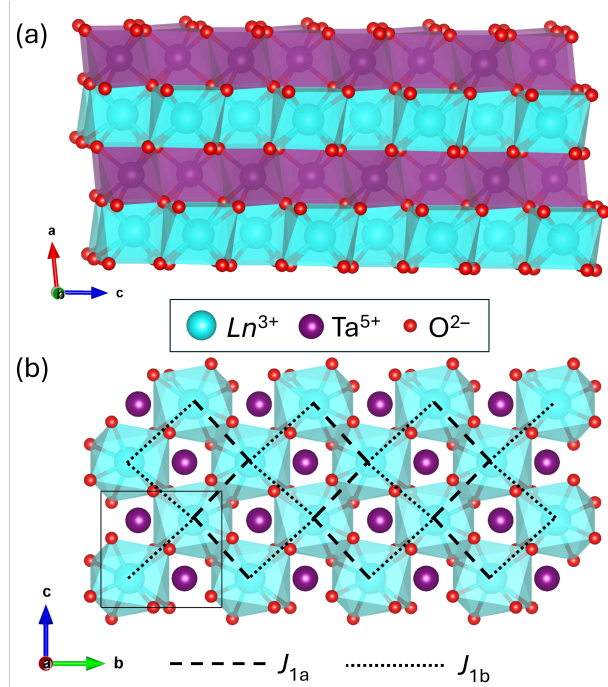


FIG. 1. Crystal structure of $M'-LnTaO_4$, space group $P2/c$ (No. 13), viewed along different crystallographic axes (b and a respectively). Blue atoms are Ln^{3+} , purple are Ta^{5+} and red are O^{2-} . In (b), dashed and dotted lines highlight the distorted square lattice of Ln^{3+} ions.

This work focuses on the lanthanide orthotantalates, LnTaO_4 , with the monoclinic M' crystal structure. The tantalates crystallise in several different structures depending on the lanthanide ion, temperature and/or pressure. Compounds of the largest lanthanides, La–Pr, have the monoclinic space group $P2_1/c$, while compounds of the later (smaller) lanthanides can form the M ($I2/a$) or M' ($P2/c$) monoclinic phases or the tetragonal T ($I4_1/a$) phase (which is only observed *in situ*) [10]. The magnetic Ln^{3+} ions in $M-LnTaO_4$ occupy a three-dimensional (3D) distorted diamond lattice, which leads to geometric magnetic frustration from the competing nearest-neighbour interactions [11, 12]. In contrast, the layered M' phase contains magnetic Ln^{3+} ions on a two-dimensional (2D) distorted square lattice, which also displays frustration.

The crystal structure of $M'-LnTaO_4$ is shown in Fig. 1. It is built from alternating layers of edge-sharing TaO_6 octahedra and LnO_8 square antiprisms, Fig. 1(a). Within each layer of lanthanide-oxygen polyhedra, the Ln^{3+} ions form a distorted square network, Fig. 1(b),

with two distinct nearest-neighbour distances, denoted J_{1a} and J_{1b} . The interlayer $Ln-Ln$ separation (e.g. 5.15 Å for M' -TbTaO₄ at room temperature) is more than 30 % longer than either of the intralayer $Ln-Ln$ distances (3.71 and 3.96 Å for M' -TbTaO₄). Therefore, we can consider this a quasi-2D system. The combination of highly localised $4f$ orbitals, a quasi-2D magnetic network, and geometric frustration makes it likely that long-range order might be partially or wholly suppressed in these materials.

Recently, two independent studies investigated frustrated magnetism in the isostructural spin- $\frac{1}{2}$ system, M' -YbTaO₄. They both determined that YbTaO₄ has a spin-orbit-driven $J_{eff} = \frac{1}{2}$ Kramers doublet ground state with a large gap to the first excited state. The Curie-Weiss temperature θ_{CW} was negative, indicating weak antiferromagnetic correlations between Yb³⁺ spins. Ramanathan *et al.* found no magnetic ordering down to 100 mK in specific heat measurements [13]. This means that the frustration index $f = |\theta_{CW}/T_N| \approx 10$, indicating strong frustration [14]. Kumar *et al.* similarly found a lack of magnetic order at $T \geq 1.8$ K; they also confirmed the presence of fluctuating Yb³⁺ spins using muon-spin relaxation (μ SR) spectroscopy [15]. The combined experimental evidence supports a quantum disordered ground state in M' -YbTaO₄.

In this study, we measure the bulk magnetic properties of the analogous lanthanide tantalate compounds with $Ln = \text{Tb, Dy, Ho and Er}$, which each have unique electronic configurations and different quantum numbers L , S and J . We find that M' -TbTaO₄ orders antiferromagnetically at 2.1 K, while the other three compounds have AFM correlations (Curie-Weiss constants ranging from -3 to -7.5 K) but do not display long-range order above 1.8 K. Neutron diffraction was used to confirm the nuclear crystal structures at room temperature for $Ln = \text{Ho and Er}$. Neutron diffraction also allowed us to track the nuclear structure of M' -TbTaO₄ as a function of temperature on cooling to 1.5 K, and to determine its magnetic structure below T_N . We find that M' -TbTaO₄ displays long-range AFM order with an ordering vector of $\vec{k} = (\frac{1}{2}, \frac{1}{2}, 0)$ and the spins directed mainly along the c -direction.

II. EXPERIMENTAL METHODS

A. Synthesis

Polycrystalline samples of $LnTaO_4$ in the monoclinic M' phase were synthesised using ceramic methods on a 0.5–4.0 g scale. The lanthanide oxides, Tb_4O_7 (99.9 %, Alfa Aesar), Dy_2O_3 (99.99 %, Alfa Aesar), Ho_2O_3 (99.99 %, Alfa Aesar) or Er_2O_3 (99.9 %, Alfa Aesar) respectively, were ground in stoichiometric ratio with Ta_2O_5 (99.993 %, Thermo Scientific) using a pestle and mortar. The powders were placed in alumina crucibles and heated in air at $3\text{ }^\circ\text{C min}^{-1}$ to 1200–1450 $^\circ\text{C}$ for 24 h (a more detailed discussion of the optimum temperature for each sample can be found in Section III A). The samples were cooled to room temperature at the natural rate of the furnace, ground and reheated with the same heating profile until the weight fractions of impurity phases no longer decreased.

B. Powder X-ray diffraction (PXRD)

Phase purity was checked using powder X-ray diffraction (PXRD) on a Bruker D8 diffractometer with $\text{Cu K}\alpha$ radiation, $\lambda = 1.541\text{ \AA}$. PXRD patterns for structural refinement were collected at the I11 beamline, Diamond Light Source [16], with wavelength (refined from a silicon standard) $\lambda = 0.82869\text{ \AA}$. Samples were mixed 1:1 by volume with ground glass to reduce absorption and packed into $\phi = 0.5\text{ mm}$ borosilicate capillaries. Rietveld refinement [17] was carried out using the program TOPAS v5 [18]. The background was fitted with a Chebyshev polynomial with 12 coefficients and the peakshape was a Voigt function with axial divergence asymmetry. During refinement, the x and z coordinates of the Ln and Ta atoms were fixed at these values representing special positions in the cell: $x_{Ln} = 0$, $z_{Ln} = 0.25$; $x_{Ta} = 0.5$, $z_{Ta} = 0.75$. The atomic coordinates of the oxygen atoms were also fixed at values taken from the literature [19]. The refined parameters included the background coefficients, zero offset, peak shape parameters, y coordinates of the Ln and Ta atoms, and isotropic thermal parameters B_{iso} for each element.

C. Powder neutron diffraction (PND)

Large samples (approximately 4 g each) of M' -TbTaO₄, M' -HoTaO₄ and M' -ErTaO₄ were investigated using time-of-flight (TOF) powder neutron diffraction (PND) at the GEM beamline [20], ISIS Neutron and Muon Source [21]. Note that M' -DyTaO₄ was excluded from the neutron diffraction study because of the very strong neutron absorption of some Dy isotopes [22] which would require isotopically enriched samples for PND experiments. The samples were packed into $\phi = 6$ mm vanadium cans and measured at 300 K (all samples) and at 100, 30 and 1.5 K (Tb only) using an ILL Orange cryostat [23]. Rietveld refinement [17] was carried out using the program TOPAS v5 [18] against banks 3–6 simultaneously, each with equal weighting.

D. Magnetometry

Magnetic measurements were made using a Quantum Design Materials Properties Measurement System (MPMS-3). Approximately 10 mg of each sample (weighed accurately in each case) was contained in clingfilm and the standard plastic sample holders then inserted into a brass sample holder. The DC magnetic moment was measured as a function of temperature upon warming in the range 1.8–300 K at a field of 500 Oe, after cooling in zero field (ZFC) or in the applied field (FC). The DC moment was also measured as a function of magnetic field in the range 0–7 T at temperatures of 2, 4, 6, 8, 10 and 100 K.

E. Specific heat

Approximately 40 mg of each sample (weighed accurately in each case) was ground with an equal mass of Ag powder (Alfa Aesar, 99.99%, –635 mesh) using a pestle and mortar, then pressed into a $\phi = 5$ mm pellet. Portions of this pellet weighing 5–20 mg were attached to the sample holder using Apiezon N grease. The heat capacity was measured at $T = 1.8$ –30 K using a Quantum Design Physical Properties Measurement System (PPMS); an initial addenda (background) measurement was made before adding the pellet, in order to subtract the heat capacity contribution arising from the grease. The Ag lattice contribution to the total heat capacity was then subtracted using values from the literature [24]. Furthermore, for each compound M' -LnTaO₄, the lattice contribution C_{latt} was modelled using the Debye

law:

$$C_{\text{latt}} = \frac{9nRT^3}{\theta_D^3} \int_0^{\frac{\theta_D}{T}} \frac{x^4 e^x}{(e^x - 1)^2} dx \quad (1)$$

where n is the number of atoms per formula unit, R is the molar gas constant, T the temperature in K, and θ_D the Debye temperature in K [25]. A scalar parameter p was substituted for $9nR$ in the fitting equation and refined to account for the sample mass error and imperfect coupling to the sample stage. The lattice contribution was then subtracted from all datasets to leave the magnetic heat capacity, $C_{\text{mag}}(T)$, for each compound. The obtained Debye temperatures were 256(2), 197(2), 127(3), and 148(2) K for $Ln = \text{Tb, Dy, Ho, and Er}$ respectively.

III. RESULTS AND DISCUSSION

A. Structural characterisation

The phase space of the lanthanide tantalates $Ln\text{TaO}_4$ contains several distinct polymorphs. For $Ln = \text{Tb–Er}$, the equilibrium phase at room temperature is M' , which on heating to around 1400 °C transforms into the tetragonal T (scheelite) phase. However, the T phase cannot be isolated at room temperature and upon cooling transforms into the M (fergusonite) phase [10, 26]. Therefore, targeted synthesis of the M' phase requires the temperature to be maintained as high as possible, to facilitate atomic diffusion, whilst not exceeding the $M' - T$ transition temperature [27, 28]. The optimum furnace temperature was found to be 1350 °C for $Ln = \text{Tb, Dy and Ho}$, and 1450 °C for $Ln = \text{Er}$. It proved impossible to stabilise phase-pure M' - GdTaO_4 (or any pure M' samples with larger lanthanide ions) because when the synthesis temperature was kept low enough to avoid forming the M phase, there was always competition from Gd_3TaO_7 [29].

The crystal structures of M' - $Ln\text{TaO}_4$ were refined against high-resolution synchrotron powder X-ray diffraction (PXRD) data using the Rietveld method. The refined parameters for all four compounds are given in Table I and the refinement plots are in the Supplemental Material, Figures S1–S4 [30]. The PXRD data showed no presence of the competing M -phase in these samples and the refined structural parameters of the four samples agree well with reports from the literature [10, 19]. Note: with respect to those literature reports, the

origin has been shifted by half a unit cell in the b direction in order to achieve consistency between the nuclear and magnetic unit cell models (see later Section IIID and Table S2 in Supplemental Material [30]).

TABLE I. Unit cell parameters for M' - Ln TaO₄ ($Ln = \text{Tb, Dy, Ho, Er}$) in space group $P2/c$. Values obtained by Rietveld refinement against synchrotron PXRD data, $T = 300$ K, $\lambda = 0.82869$ Å.

	M' -TbTaO ₄	M' -DyTaO ₄	M' -HoTaO ₄	M' -ErTaO ₄
a (Å)	5.14126(4)	5.12917(2)	5.11433(2)	5.09892(4)
b (Å)	5.48935(4)	5.47022(3)	5.45273(2)	5.43875(5)
c (Å)	5.33646(4)	5.31716(2)	5.30149(2)	5.28448(5)
β (°)	96.6668(5)	96.5857(3)	96.5011(2)	96.4289(4)
V (Å ³)	149.588(2)	148.203(1)	146.893(1)	145.626(2)
y_{Ln}	0.73406(16)	0.73436(15)	0.73385(13)	0.73369(18)
y_{Ta}	0.80846(15)	0.80704(14)	0.80600(12)	0.80578(17)
χ^2	3.68	3.98	4.72	4.21
R_{wp} (%)	2.65	2.93	3.26	2.88

Further structural characterisation was carried out using powder neutron diffraction (PND) on three samples, M' -TbTaO₄, HoTaO₄ and ErTaO₄ [21]. Fig. 2 shows the Rietveld refinement for room-temperature data on M' -TbTaO₄; plots of the refinements for the other two compounds are presented in the Supplemental Material [30]. Both PXRD and PND on the neutron samples showed small amounts (≤ 1 wt %) of impurities: $Ln_3\text{TaO}_7$ [28, 29]; the competing M phase of TbTaO₄; and Ta₂O₅ in the Ho sample, which unfortunately could not be eliminated after repeated firing of the larger neutron samples. However, all magnetometry and heat capacity measurements were done on smaller samples which were found to be phase-pure by high-resolution synchrotron PXRD. Unlike with PXRD, the relative neutron scattering lengths [22] permitted refinement of the fractional coordinates of O ions as well as those of the metal ions in our samples, and the refined values (Table II) matched those reported in the literature [19]. The unit cell volumes are linearly related to the lanthanide ionic radius [31] and are consistent with literature reports, as shown by Fig. 3.

PND was also measured on the sample of M' -TbTaO₄ at low temperatures using a cryostat. Upon cooling, the a , b and c lattice parameters decreased while the angle β increased.

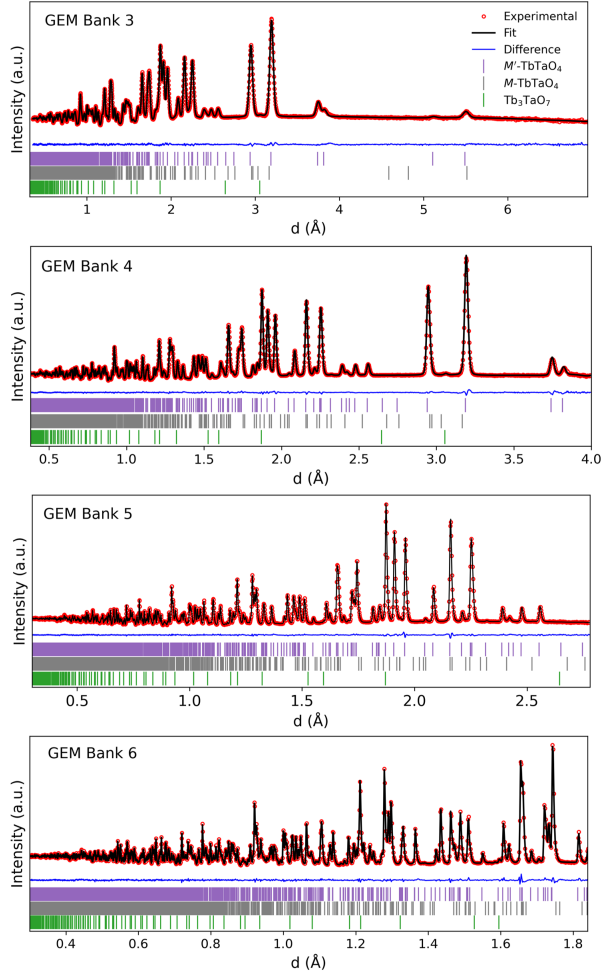


FIG. 2. Rietveld refinement against room-temperature TOF PND data for M' -TbTaO₄.

Overall, the unit cell volume decreased by less than 0.5 % between 300 and 1.5 K. The contraction of the unit cell is as expected for normal thermal expansion behaviour and no anomalous movements of the atomic positions were detected. The Supplemental Material [30] includes a table of the refined lattice parameters, Table S1, and plots of lattice parameters (Fig. S9) and metal-oxygen bond lengths (Fig. S10) as a function of T . At 1.5 K, large new peaks appeared which indicated long-range magnetic order in M' -TbTaO₄; the magnetic structure is discussed in Section III D.

B. Magnetic measurements

Peaks in the magnetic susceptibility were visible for M' -TbTaO₄ and M' -DyTaO₄ at approximately 2.7 K for both samples (Fig. 4). There was no divergence between the zero-field-

TABLE II. Refined structural data for M' - Ln TaO₄ ($Ln = Tb, Ho, Er$) at room temperature from time-of-flight PND data (GEM, banks 3–6). Space group: $P2/c$. $Ln1$ atom at $(0, y_{Ln}, 0.25)$; Ta1 atom at $(0.5, y_{Ta}, 0.75)$.

		Tb	Ho	Er
a (Å)		5.14258(2)	5.11201(3)	5.1007(15)
b (Å)		5.49176(2)	5.45320(3)	5.4432(15)
c (Å)		5.33763(2)	5.29881(3)	5.2864(15)
β (°)		96.6566(3)	96.4658(5)	96.4040(5)
V (Å ³)		149.728(1)	146.774(1)	145.86(7)
$Ln1$	y	0.73439(5)	0.73414(7)	0.73380(7)
Ta1	y	0.80767(6)	0.80476(7)	0.80471(8)
O1	x	0.74789(5)	0.74879(7)	0.74955(7)
	y	0.41318(5)	0.41620(7)	0.41672(7)
	z	0.39731(5)	0.39987(8)	0.40129(8)
O2	x	0.27091(6)	0.26904(8)	0.26824(8)
	y	0.06469(5)	0.06442(7)	0.06462(7)
	z	0.49543(6)	0.49575(8)	0.49621(8)
B_{iso} (Å ²)	Ln	0.229(4)	0.148(5)	0.328(7)
	Ta	0.218(4)	0.200(6)	0.281(7)
	O	0.430(3)	0.418(4)	0.498(5)
R_{wp} (%)		1.41	1.73	1.83
χ^2		3.19	3.34	2.29
Impurities		0.47 wt % Tb ₃ TaO ₇ , 1.06 wt % M -TbTaO ₄	2.7 wt % Ho ₃ TaO ₇ , 1.1 wt % Ta ₂ O ₅	0.8 wt % Er ₃ TaO ₇

cooled (ZFC) and field-cooled (FC) susceptibility data which might have indicated spin-glass behaviour. This, combined with the shape of the peak for M' -TbTaO₄ suggests a transition from paramagnetism to a long-range-ordered antiferromagnetic (AFM) state upon cooling. The peak for M' -DyTaO₄ is significantly broader, which may indicate that below 2.7 K the magnetic moments have a short correlation length. Furthermore, the shape of the derivative

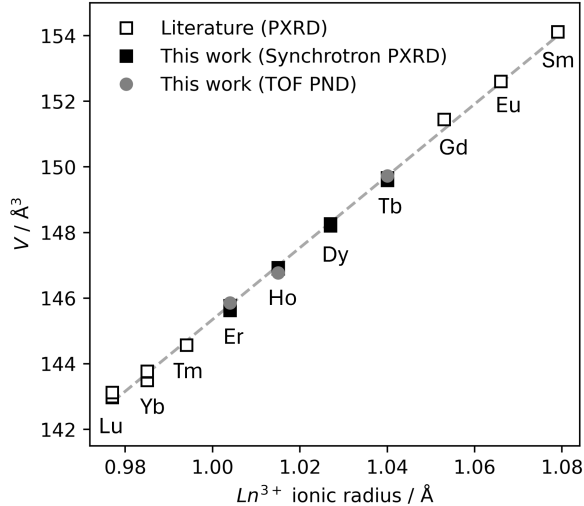


FIG. 3. Unit cell volume of M' - $Ln\text{TaO}_4$ as a function of 8-coordinate Ln^{3+} ionic radius [31] from Rietveld refinements against both high-resolution X-ray and neutron diffraction data. Error bars are smaller than the datapoints. Literature data taken from references [10, 15, 27, 32, 33].

$d(\chi T)/dT$ [34] shows a clear feature for M' - TbTaO_4 but not for M' - DyTaO_4 (Supplemental Material, Fig. S12 [30]), despite the peaks in $\chi(T)$ occurring at similar temperatures for the two compounds. Meanwhile, M' - HoTaO_4 and M' - ErTaO_4 show only Curie-Weiss behaviour with no susceptibility peaks visible in the temperature range measured.

The magnetic susceptibility $\chi = M/H$ was fitted to the modified Curie-Weiss law:

$$\chi = \chi_0 + \frac{C}{T - \theta_{CW}} \quad (2)$$

where χ_0 is a small temperature-independent susceptibility, C is the Curie constant ($C = \mu_{eff}^2/8$), and θ_{CW} is the Curie-Weiss temperature. All chemical elements and compounds have a negative, temperature-independent diamagnetic contribution to the susceptibility, χ_{Di} , which can be estimated using Pascal's constants [35] as $-8 \times 10^{-5} \text{ emu mol}^{-1}$ for these four M' - $Ln\text{TaO}_4$ compounds. However, diamagnetism is a weak effect and is typically overridden by stronger magnetic effects such as paramagnetism [36], so lanthanide-containing solids are expected to have positive values of χ_0 . We used a Nelder-Mead optimisation method (Supplemental Material, Fig. S13 [30]) to find the best linear fit to the inverse susceptibility as a function of temperature. This approach minimises the scaled least-squares difference between $(T - \theta)/C$ and $(\chi - \chi_0)^{-1}$, which is more effective than regular Curie-Weiss fitting with free parameters on both sides of the equation (eqn 2). This yielded small

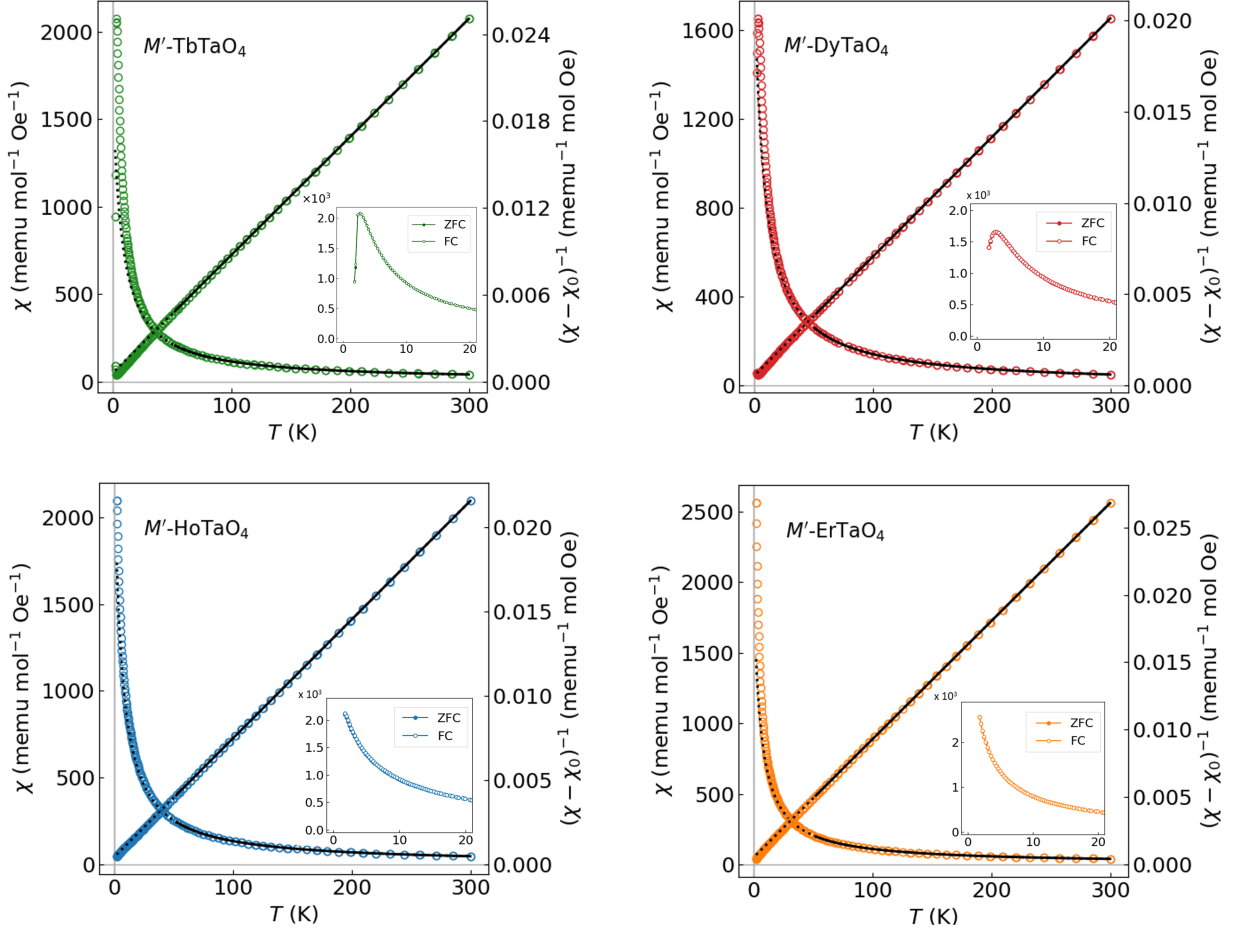


FIG. 4. Magnetic susceptibility χ and inverse susceptibility $(\chi - \chi_0)^{-1}$, fitted to the Curie-Weiss law in the range 50–300 K (black lines), for the four $M'-LnTaO_4$ compounds in this study. The black dashed lines show the extrapolation of the fit below 50 K. Insets show the low-temperature region.

positive values of χ_0 which are given in Table III along with the fitted values of θ_{CW} and μ_{eff} . Fig. 4 shows the Curie-Weiss fits as black solid lines with extrapolation below 50 K as dashed lines. The negative Curie-Weiss temperatures indicate antiferromagnetic interactions and the effective magnetic moments μ_{eff} agree quite well with the expected moments for free ions, $\mu = g_J \sqrt{J(J+1)}$.

Magnetic isotherms were measured for all samples at $T = 2, 4, 6, 8, 10$ and 100 K and are shown in Fig. 5. At $T \leq 10$ K and at high fields, the magnetisation saturates to a straight line representing the underlying paramagnetism or crystal electric field (CEF) effects. The data at $T = 2$ K were therefore fitted to a linear function between 5 and 7 T and the line was

TABLE III. Magnetic parameters for M' - Ln TaO₄ ($Ln = \text{Tb, Dy, Ho, Er}$) from Curie-Weiss fitting in the range 50–300 K.

	M' -TbTaO ₄	M' -DyTaO ₄	M' -HoTaO ₄	M' -ErTaO ₄
Sample mass (mg)	6.2	7.6	6.8	10.8
θ_{CW} (K)	-3.50(12)	-6.75(7)	-5.12(2)	-3.93(5)
μ_{eff} (μ_{B})	9.65(6)	10.93(3)	10.58(11)	9.41(3)
Free-ion moment (μ_{B})	9.72	10.65	10.61	9.58
χ_0 (emu mol ⁻¹ Oe ⁻¹)	2.0×10^{-3}	6.9×10^{-4}	1.3×10^{-3}	2.5×10^{-3}

extrapolated back to zero field (grey dashed line) to obtain an estimate for the saturation magnetisation, M_{sat} . The magnitude of M_{sat} can be compared with the predicted value ($g_J \cdot J$ for Heisenberg, $g_J \cdot J/2$ for Ising, or $2g_J \cdot J/3$ for XY anisotropy, in powder samples [37]) to give an indication of the single-ion anisotropy in these systems. The data indicate that all compounds exhibit significant single-ion anisotropy, and in particular that M' -HoTaO₄ may be an Ising system ($M_{\text{sat}} = 5$ and $g_J \cdot J = 10 \mu_{\text{B}}/\text{f.u.}$) and M' -ErTaO₄ an XY system ($M_{\text{sat}} = 6$ and $g_J \cdot J = 9 \mu_{\text{B}}/\text{f.u.}$). However, errors arising from the extrapolation and/or the sample mass mean that caution should be exercised in drawing these conclusions from the $M(H)$ data alone. For example, the magnitude of M_{sat} for M' -TbTaO₄ lies somewhat between the expected values for Ising and XY anisotropy, yet the neutron diffraction data (Section III D) indicate an almost easy-axis (Ising) behaviour. Additional neutron diffraction down to lower temperatures on the Ho and Er samples, and/or an isotopically enriched Dy sample, would be required to confirm the type of anisotropy. Spectroscopic measurements to determine the CEF levels would also provide information on anisotropy.

C. Specific heat

The zero-field magnetic specific heat for M' -TbTaO₄ is given in Fig. 6. A sharp λ -type transition is observed at $T = 2.1$ K, indicating long-range AFM ordering. The temperature of the peak in heat capacity is lower than that observed in the magnetic susceptibility (2.7 K), which is similar behaviour to the other polymorph of this compound, M -TbTaO₄ [11]. In addition, a peak in $d(\chi T)/dT$ occurs at the same temperature as the peak in the specific heat

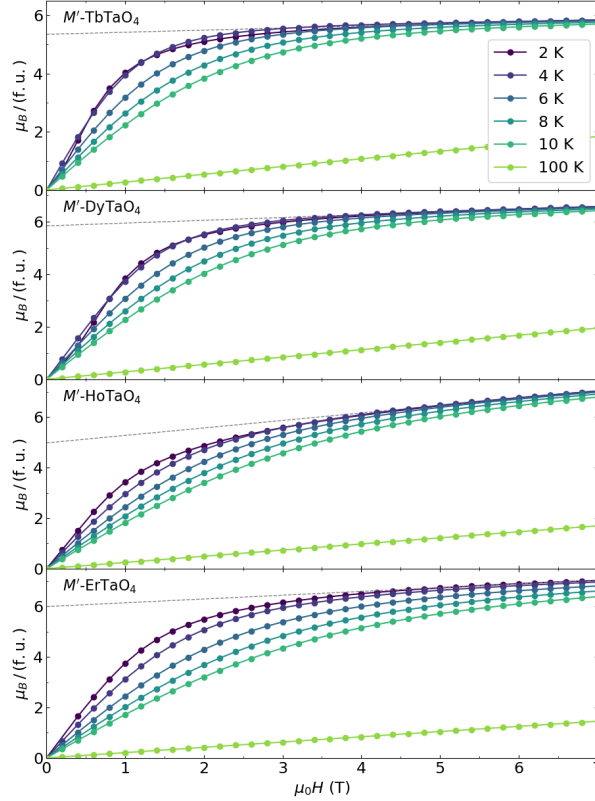


FIG. 5. Magnetic isotherms for $M'-LnTaO_4$. The dashed lines show the linear fits in the region 5-7 T, extrapolated back to 0 T.

(Supplemental Material, Fig. S12 [30]), which is typical for antiferromagnets [34]. Integration of C_{mag}/T yields the magnetic entropy, ΔS_{mag} , which approaches $4 \text{ J K}^{-1} \text{ mol}_{\text{Tb}}^{-1}$ at 30 K. This value is less than 20 % of the expected $\Delta S_{\text{mag}} = R \ln(2J + 1) = 21.32 \text{ J K}^{-1} \text{ mol}^{-1}$ ($J = 6$); clearly, since the lower-temperature side of the λ -like peak is incomplete, there is still significant further entropy to be lost on cooling the material below 1.8 K. The specific heat in zero field and applied fields (1, 2, 4 and 9 T) is also shown in Fig. 7, top right. Upon application of a magnetic field, the sharp peak is suppressed and becomes a broad feature which moves to higher temperatures with increasing field.

In contrast, for $M'-DyTaO_4$ no such sharp peak is observed (Fig. 7, top right), which agrees with the absence of a peak in $d(\chi T)/dT$ [34] (Supplemental Material, Fig. S12 [30]). There is no evidence for either long-range order or spin freezing above 1.8 K in either the zero-field or 1 T specific heat data. At 2 T we observe a broad peak, centred around 5 K. This peak then shifts to higher temperatures as the field increases, which is typical of a

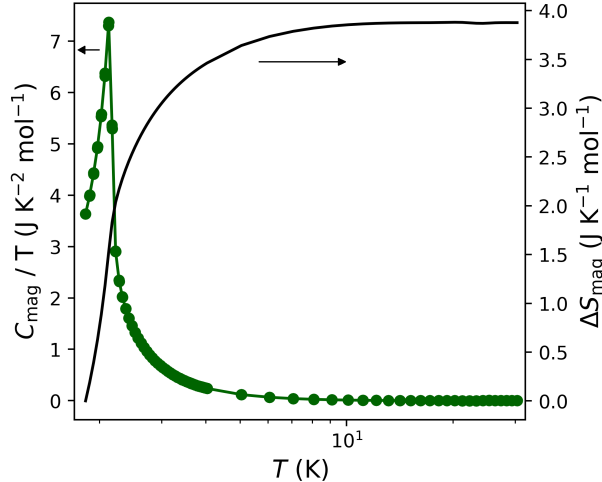


FIG. 6. M' -TbTaO₄ magnetic specific heat data (left axis) and magnetic entropy change (right axis).

Schottky anomaly. Such behaviour arises from Zeeman splitting of a Kramers doublet state with $J_{\text{eff}} = \frac{1}{2}$, as observed in the isostructural M' -YbTaO₄ at all fields [15]. However, the absence of a peak in the lower-field datasets suggests that the ground state at zero field is not a Kramers doublet, and that there is a field-induced transition between 1 and 2 T, perhaps reflecting suppression of the short-range order suggested by the magnetic susceptibility. In Fig. 5 the magnetisation curves for M' -DyTaO₄ at 2 K and 4 K cross over twice at low fields, which also hints at magnetic ordering. There are also two small anomalies in the M' -DyTaO₄ data around $T = 20$ and 25 K whose origin is unknown. They may be an artefact of measurements or related to the sample environment, because less pronounced features appear at the same temperatures in the HoTaO₄ and ErTaO₄ data and they are independent of the applied field.

Like Dy³⁺ ions, Er³⁺ ions have an odd number of electrons and are therefore also Kramers ions. M' -ErTaO₄ displays a Schottky-like peak similar to that of M' -DyTaO₄ (Fig. 7, bottom right) but, unlike DyTaO₄, this behaviour appears to extend to the lowest fields. There is a second broad feature between around 7 and 22 K in the zero-field data, which seems to be suppressed in applied magnetic fields and may represent short-range magnetic correlations; the feature might be investigated in the future using neutron diffraction and/or inelastic scattering in this temperature range.

Finally, the specific heat data for M' -HoTaO₄ are shown in Fig. 7 (bottom left). A

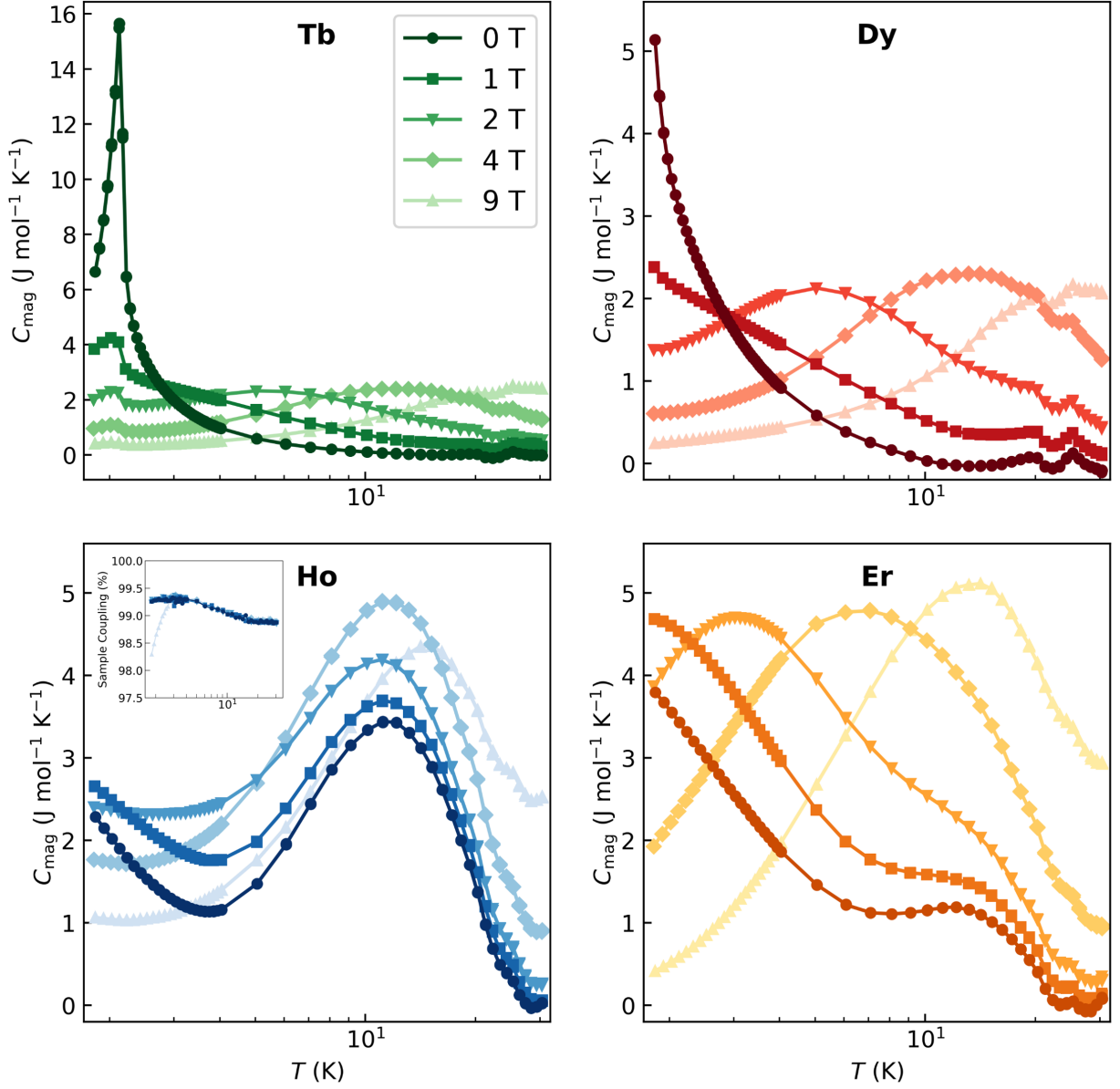


FIG. 7. Magnetic specific heat data at various applied fields for the four M' - Ln TaO₄ samples. Inset for $Ln = \text{Ho}$ shows the sample coupling.

broad hump centred around 8 K is clearly visible and, with the exception of the 9 T data, the temperature of the maximum remains fairly independent of applied field, unlike in the Dy and Er analogues. Broad features like this have been observed in other compounds containing Ho^{3+} (a non-Kramers ion), especially when the Ho^{3+} ions are in low-symmetry crystallographic environments; in π - HoBO_3 the behaviour was ascribed to a non-magnetic singlet ground state, with the broad feature arising from van Vleck paramagnetism [38].

In M' -HoTaO₄, the Ho³⁺ ion is on the $2e$ Wyckoff position of space group 13 ($P2/c$) with site symmetry C_2 . The low site symmetry and non-Kramers nature of Ho³⁺ mean that its $2J+1 = 15$ -fold degeneracy may be lifted by interaction with the surrounding CEF, i.e. there is no symmetry-enforced ground state doublet, unlike in many Er³⁺ or Yb³⁺ compounds. Hence, we suggest that the specific heat data on M' -HoTaO₄ represent a singlet ground state. The higher-temperature peak in the 9 T dataset is probably an anomaly, related to some slippage of the sample platform or thermocouples between the 4 T and 9 T measurements, since there is no evidence in the $M(H)$ data for a field-induced transition in this range. The inset to Fig. 7 shows how the sample coupling for M' -HoTaO₄ is different for the 9 T data at low temperatures, supporting this hypothesis; for the other three compounds, the sample coupling had a slight T -dependence but was independent of applied field.

D. Magnetic structure of M' -TbTaO₄

The magnetic structure of M' -TbTaO₄ was investigated using PND [21] below the ordering temperature of $T_N = 2.1$ K. Additional peaks appeared between the 30 K and 1.5 K datasets in positions which indicated commensurate magnetic ordering. Using the FullProf Suite [39], a suitable magnetic ordering vector was found to be $\vec{k} = (\frac{1}{2}, \frac{1}{2}, 0)$. The magnetic peaks were then modelled in TOPAS v5 [18] in magnetic space group 14.80 (P_a2_1/c). Each Tb³⁺ ion carries a magnetic moment with refined components $-0.702(8)$, 0 and $8.053(6)$ μ_B along the a , b and c axes respectively. This corresponds to $-1.652(12)$, 0 and $7.996(6)$ μ_B in Cartesian axes and an ordered moment magnitude of $8.17(9)$ μ_B . This is consistent with the expectation of $g_J J = 9$ μ_B for Tb³⁺ ions. Note that this magnetic space group does permit a non-zero y -component to the magnetic moment. However, its value always refined to zero (from different trial starting points) with a large uncertainty reported by the TOPAS software, so it was subsequently fixed at zero. Thus, in this model, the magnetic moments are primarily directed along the c -direction and are fractionally canted towards a . The nearest-neighbour magnetic moments are coupled antiferromagnetically within the bc plane, and the next-nearest-neighbour interactions are ferromagnetic, creating a zigzag-like ordering pattern. Adjacent layers along the a axis are coupled antiferromagnetically.

The magnetic structure model for M' -TbTaO₄ is shown in Fig. 8(a) and (b), and the Rietveld refinement at 1.5 K (bank 3) in Fig. 8(c). Rietveld refinements for all banks

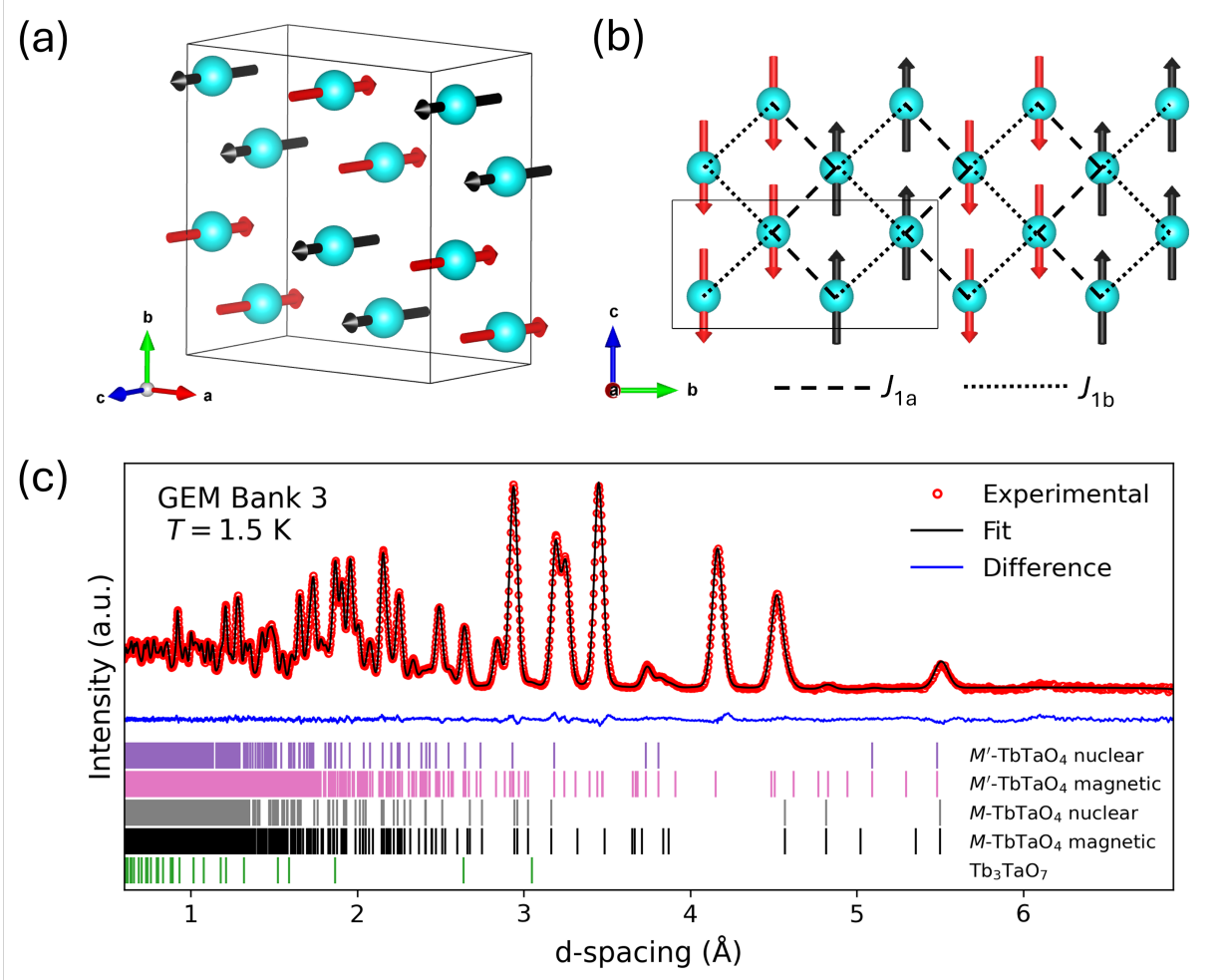


FIG. 8. (a) Magnetic structure model for one magnetic unit cell of M' -TbTaO₄ at 1.5 K. (b) Magnetic structure model for a single layer (distorted square lattice). Dashed lines are the nearest-neighbour distances at 3.7054(4) Å, dotted lines are the next-nearest-neighbour distances at 3.9493(4) Å. (c) Rietveld refinement against TOF PND data at $T = 1.5$ K: GEM bank 3.

are available in the Supplemental Material, Figure S11 [30], along with a table giving the structural parameters for a one-phase combined nuclear and magnetic structure, Table S2. In addition to the M' -TbTaO₄, two other minor phases contribute intensity to the 1.5 K neutron diffraction pattern: 1.06 wt % M -TbTaO₄ (both nuclear and magnetic reflections [11]), and 0.47 wt % Tb₃TaO₇. Tb₃TaO₇ is known to undergo two magnetic ordering transitions at 2.9 K and 3.6 K [29], which may be the origin of the very small regions of unindexed intensity in the 1.5 K data. However, the magnetic structure of Tb₃TaO₇ has not been reported and could not be deduced from our data because of the very low weight fraction of Tb₃TaO₇ in

this sample.

In comparison to the M' phase described above, the M polymorph of TbTaO_4 , which has a three-dimensional “stretched diamond” network of Tb^{3+} ions, displays AFM order below $T_N = 2.25$ K with the moments directed along the a -axis [11]. Both phases of TbTaO_4 display almost easy-axis anisotropy and antiferromagnetic coupling between nearest-neighbour Tb ions. However, differences in their crystal structures lead to important differences in the magnetic structures. In the M phase, there are four near-neighbour AFM interactions at similar distances ($2 \times J_{1a}$ at 3.75 Å, $2 \times J_{1b}$ at 3.84 Å) and the closest ferromagnetically coupled pair of spins are much further apart at ~ 5.05 Å. In contrast, the M' phase has AFM $2 \times J_{1a}$ at 3.71 Å and FM $2 \times J_{1b}$ at 3.95 Å, plus AFM inter-layer coupling J_2 (5.13 Å). The tilting of the magnetic moments out of the plane in the M' phase might be a way to partially relieve the frustration that arises from these competing AFM and FM near-neighbour interactions. The experimental T_N is slightly lower for the M' phase than the M phase (2.1 vs 2.25 K). However, the Curie-Weiss temperature is smaller for M' than M , and the estimated frustration parameter $f = |\theta_{\text{CW}}/T_N|$ is therefore also smaller, although both values are modest (M : $f \approx 4.2$, M' : $f \approx 1.7$). We can use mean-field estimates of the nearest-neighbour exchange (J_{nn}) and dipolar (D_{nn}) interactions, equations 3 and 4, to rationalise the difference in magnetic ordering temperatures:

$$J_{\text{nn}} = \frac{3k_B|\theta_{\text{CW}}|}{2nJ(J+1)} \quad (3)$$

$$D_{\text{nn}} = \frac{\mu_0\mu_{\text{eff}}^2}{4\pi R^3J(J+1)} \quad (4)$$

where n is the number of “nearest neighbours” and J is the total angular momentum quantum number, $J = 6$ for Tb^{3+} . We took $n = 4$ for both structures; for R_{nn} we used an average of the four closest Tb–Tb distances, which are within 7 % of each other (compared with the next closest ion, which is at a distance more than 30 % larger than R_{nn} in both phases). In M' - TbTaO_4 , its smaller Curie-Weiss temperature and greater average Tb–Tb separation lead to smaller values for both the superexchange and dipolar interactions. These weaker interactions are reflected in the slightly lower magnetic ordering temperature. Table IV gives the relevant parameters and estimated interaction strengths for all four samples of M' - LnTaO_4 with comparisons to the M polymorphs [11]. For each pair of compounds

with the same Ln , the values of J_{nn} and D_{nn} are smaller for the M' phase than for the M phase. We note that the difference in D_{nn} for M' versus M gets smaller across the lanthanide series (as the average $Ln-Ln$ distance, R , gets smaller), until D_{nn} is the same for M - and M' - $ErTaO_4$. This demonstrates an interesting correlation with the minimum Ln^{3+} radius, below which the M phase can no longer be synthesised under ambient pressure conditions [10, 40]. The use of pressure to produce compounds (magnetic or non-magnetic) which are inaccessible by conventional synthesis methods is well documented [41] but typically limited to small volumes of polycrystalline samples. However, the application of a magnetic field during synthesis has lately been revealed as another possible control parameter for synthesis. Under the so-called magneto-synthesis, large single crystals of $BaIrO_3$ were produced with different structures and magnetic behaviour depending on the field applied during crystal growth [42]. The lanthanide tantalates, with their range of different crystal structures and magnetic properties, may be good candidates for future investigations into the wider applicability of this technique.

TABLE IV. Estimates of the nearest-neighbour exchange and dipolar interactions for M' - and M - $LnTaO_4$ ($Ln = Tb, Dy, Ho, Er$). The Curie-Weiss temperatures and effective magnetic moments for the M phase are taken from ref. 11.

	TbTaO ₄		DyTaO ₄		HoTaO ₄		ErTaO ₄	
	M	M'	M	M'	M	M'	M	M'
θ_{CW} (K)	-9.49	-3.50	-6.88	-3.0	-7.84	-6.38	-7.43	-6.05
μ_{eff} (μ_B)	10.18	9.65	10.71	10.64	10.57	10.66	9.44	9.55
n	4	4	4	4	4	4	4	4
J	6	6	7.5	7.5	8	8	7.5	7.5
R_{nn} (Å)	3.799	3.830	3.786	3.816	3.775	3.805	3.763	3.794
J_{nn} (K)	0.0847	0.0313	0.0405	0.0176	0.0408	0.0332	0.0437	0.0356
D_{nn} (K)	0.0280	0.0246	0.0207	0.0199	0.0180	0.0179	0.0163	0.0163

Notably, both phases of $TbTaO_4$ are the only compounds in their respective $M'-LnTaO_4$ ($Ln = Tb-Yb$) or $M-LnTaO_4$ series ($Ln = Nd-Yb$) which have been found to display long-range order above 1.8 K. Ramanathan *et al.* reported that $M'-YbTaO_4$ has no long-range order down to 0.1 K, but to our knowledge no other compounds in this family have been

studied below 1.8 K. Further low-temperature experiments on the other $LnTaO_4$ compounds should be carried out where possible, to compare and contrast between different lanthanide ions and to determine whether there is any correlation between the Néel temperatures or magnetic structures of the M and M' phases for lanthanide ions other than Tb^{3+} .

IV. CONCLUSIONS

We have investigated the crystal structure and bulk magnetic properties of the lanthanide tantalum oxides, $M'-LnTaO_4$, where $Ln = Tb, Dy, Ho$ and Er . Powder X-ray and neutron diffraction were used to study the crystal structure. Using magnetometry and heat capacity measurements, we observe LRO at $T_N = 2.1$ K for $TbTaO_4$ and no LRO above 1.8 K for the compounds where $Ln = Dy, Ho$ or Er , although the susceptibility of $M'-DyTaO_4$ suggests possible short-range magnetic ordering below $T \approx 2.7$ K. $M'-ErTaO_4$ has a Kramers doublet ground state as evidenced by the Schottky-type anomaly in field-dependent specific heat data, similar to the previously reported $M'-YbTaO_4$. A similar feature was seen for $M'-DyTaO_4$ above 2 T, but there was no peak in the heat capacity at lower fields. This behaviour could be related to short-range order and/or CEF effects.

Powder neutron diffraction indicates that the magnetic moments in $M'-TbTaO_4$ below T_N are directed primarily along the c -axis in a long-range antiferromagnetic structure with $\vec{k} = (\frac{1}{2}, \frac{1}{2}, 0)$, with an ordered magnitude of $8.17(9) \mu_B$ at 1.5 K. We compared the magnetic ordering temperatures of the M and M' polymorphs of $TbTaO_4$ and related these to the estimated strengths of superexchange and dipolar coupling between Tb^{3+} ions. For all Ln , the interactions are weaker for the M' phase than for the M phase, which correlates with the smaller T_N for M' - vs M - $TbTaO_4$. This work provides insight into how the magnetic anisotropy and ordering behaviour of rare-earth oxides may be significantly affected, either by substitution of different magnetic ions into a given crystal structure, or by differences in the crystal structure for a given magnetic ion (specifically Tb^{3+}). Future investigations at sub-kelvin temperatures will enable us to extend this work to other lanthanide ions.

ACKNOWLEDGMENTS

We acknowledge funding from the EPSRC for the use of the Advanced Materials Characterisation Suite (EP/M000524/1). N.D.K. acknowledges funding from Jesus College, Cambridge for a Research Fellowship. S.E.D. acknowledges funding from the EPSRC (EP/T028580/1). We acknowledge I11 beamline at the Diamond Light Source, UK, for the synchrotron XRD measurement done under BAG proposal CY40166-2, and thank Farheen N. Sayed for organising the beamtime. Data collection at the ISIS Neutron and Muon Source was supported by a beamtime allocation RB2520021 from the Science and Technology Facilities Council [21]. We thank James M. A. Steele and Jeongjae Lee for assistance with neutron data collection.

Research data supporting the findings of this study will be made openly available at <https://doi.org/10.17863/CAM.125160> [43].

-
- [1] P. W. Anderson, The resonating valence bond state in La_2CuO_4 and superconductivity, *Science* **235**, 1196 (1987).
 - [2] J. E. Greedan, Geometrically frustrated magnetic materials, *J. Mater. Chem.* **11**, 37 (2001).
 - [3] J. R. Chamorro, T. M. McQueen, and T. T. Tran, Chemistry of Quantum Spin Liquids, *Chem. Rev.* **121**, 2898 (2021).
 - [4] P. Park, G. Sala, T. Proffen, M. B. Stone, A. D. Christianson, and A. F. May, Quantum magnetism in the frustrated square lattice oxyhalides YbBi_2IO_4 and $\text{YbBi}_2\text{ClO}_4$, *Phys. Rev. B* **109**, 014426 (2024).
 - [5] M. Watanabe, N. Kurita, H. Tanaka, W. Ueno, K. Matsui, T. Goto, and M. Hagihala, Contrasting magnetic structures in SrLaCuSbO_6 and SrLaCuNbO_6 : Spin- $\frac{1}{2}$ quasi-square-lattice $J_1 - J_2$ Heisenberg antiferromagnets, *Phys. Rev. B* **105**, 054414 (2022).
 - [6] A. H. Abdeldaim, T. Li, L. Farrar, A. A. Tsirlin, W. Yao, A. S. Gibbs, P. Manuel, P. Lightfoot, G. J. Nilsen, and L. Clark, Realising square and diamond lattice $S=1/2$ Heisenberg antiferromagnet models in the α and β phases of the coordination framework, $\text{KTi}(\text{C}_2\text{O}_4)_2 \cdot x\text{H}_2\text{O}$, *Phys. Rev. Mater.* **4**, 104414 (2020).
 - [7] O. Mustonen, S. Vasala, E. Sadrollahi, K. P. Schmidt, C. Baines, H. C. Walker, I. Terasaki,

- F. J. Litterst, E. M. Baggio-Saitovitch, and M. Karppinen, Spin-liquid-like state in a spin-1/2 square-lattice antiferromagnet perovskite induced by d^{10} - d^0 cation mixing, *Nat. Commun.* **9**, 1085 (2018).
- [8] O. Mustonen, S. Vasala, K. P. Schmidt, E. Sadrollahi, H. C. Walker, I. Terasaki, F. J. Litterst, E. Baggio-Saitovitch, and M. Karppinen, Tuning the $S=1/2$ square-lattice antiferromagnet $\text{Sr}_2\text{Cu}(\text{Te}_{1-x}\text{W}_x)\text{O}_6$ from Néel order to quantum disorder to columnar order, *Phys. Rev. B* **98**, 064411 (2018).
- [9] S. Guchhait, A. Painganoor, S. S. Islam, J. Sichelschmidt, M. D. Le, N. B. Christensen, and R. Nath, Magnetic and crystal electric field studies of the rare earth based square lattice antiferromagnet NdKNaNbO_5 , *Phys. Rev. B* **110**, 144434 (2024).
- [10] L. H. Brixner and H. Y. Chen, On the Structural and Luminescent Properties of the M' LnTaO_4 Rare Earth Tantalates, *J. Electrochem. Soc.* **130**, 2435 (1983).
- [11] N. D. Kelly, L. Yuan, R. L. Pearson, E. Suard, I. Puente Orench, and S. E. Dutton, Magnetism on the stretched diamond lattice in lanthanide orthotantalates, *Phys. Rev. Mater.* **6**, 044410 (2022).
- [12] X. Zhang, N. D. Kelly, D. Sheptyakov, C. Liu, S. Deng, S. S. Saxena, and S. E. Dutton, Magnetoelastic coupling in the stretched diamond lattice of TbTaO_4 , *Mater. Adv.* **6**, 2570 (2025).
- [13] A. Ramanathan, M. Mourigal, and H. S. La Pierre, Frustrated Magnetism and Spin Anisotropy in a Buckled Square Net YbTaO_4 , *Inorg. Chem.* **64**, 158 (2024).
- [14] A. P. Ramirez, Strongly geometrically frustrated magnets, *Annu. Rev. Mater. Sci.* **24**, 453 (1994).
- [15] J. Kumar, R. Roy, D. Ranaut, J. G. Nakamura, S. Kanungo, and K. Mukherjee, YbTaO_4 : A quasi-two-dimensional frustrated magnet possessing spin orbit entangled Kramers doublet ground state, *Phys. Rev. B* **110**, 174420 (2024).
- [16] S. P. Thompson, J. E. Parker, J. Potter, T. P. Hill, A. Birt, T. M. Cobb, F. Yuan, and C. C. Tang, Beamline I11 at Diamond: A new instrument for high resolution powder diffraction, *Rev. Sci. Instrum.* **80**, 075107 (2009).
- [17] H. M. Rietveld, A profile refinement method for nuclear and magnetic structures, *J. Appl. Crystallogr.* **2**, 65 (1969).
- [18] A. A. Coelho, TOPAS and TOPAS-Academic: An optimization program integrating computer

- algebra and crystallographic objects written in C++, J. Appl. Crystallogr. **51**, 210 (2018).
- [19] I. Hartenbach, F. Lissner, T. Nikelski, S. F. Meier, H. Müller-Bunz, and T. Schleid, Über oxotantalate der lanthanide des formeltyps $MTaO_4$ ($M = La - Nd, Sm - Lu$), Zeitschrift für Anorg. und Allg. Chemie **631**, 2377 (2005).
- [20] A. C. Hannon, Results on disordered materials from the GEneral Materials diffractometer, GEM, at ISIS, Nucl. Instruments Methods Phys. Res. A **551**, 88 (2005).
- [21] N. D. Kelly, J. Lee, J. M. A. Steele, S. E. Dutton, and I. da Silva, $M'-LnTaO_4$: a model for the 2D square lattice of magnetic ions, STFC ISIS Neutron and Muon Source 10.5286/ISIS.E.RB2520021 (2025).
- [22] V. F. Sears, Neutron scattering lengths and cross sections, Neutron News **3**, 26 (1992).
- [23] D. Brochier, Cryostat à température variable pour mesures neutroniques ou optiques, ILL Technical Report 77/74 (1977).
- [24] D. Smith and F. Fickett, Low-Temperature Properties of Silver, J. Res. Natl. Inst. Stand. Technol. **100**, 119 (1995).
- [25] E. S. R. Gopal, *Specific Heats at Low Temperatures* (Springer US, Boston, MA, 1966).
- [26] S. A. Mather and P. K. Davies, Nonequilibrium Phase Formation in Oxides Prepared at Low Temperature: Fergusonite-Related Phases, J. Am. Ceram. Soc. **78**, 2737 (1995).
- [27] B. G. Mullens, M. Saura-Múzquiz, F. P. Marlton, M. Avdeev, H. E. A. Brand, S. Mondal, G. Vaitheeswaran, and B. J. Kennedy, Beyond the ionic radii: A multifaceted approach to understand differences between the structures of $LnNbO_4$ and $LnTaO_4$ fergusonites, J. Alloys Compd. **930**, 167399 (2023).
- [28] B. G. Mullens, M. Saura-Múzquiz, G. Cordaro, F. P. Marlton, H. E. Maynard-Casely, Z. Zhang, G. Baldinozzi, and B. J. Kennedy, Variable Temperature In Situ Neutron Powder Diffraction and Conductivity Studies of Undoped $HoNbO_4$ and $HoTaO_4$, Chem. Mater. **36**, 5002 (2024).
- [29] M. Wakeshima, H. Nishimine, and Y. Hinatsu, Crystal structures and magnetic properties of rare earth tantalates RE_3TaO_7 ($RE =$ rare earths), J. Phys. Condens. Matter **16**, 4103 (2004).
- [30] See Supplemental Material at [URL] for additional Rietveld refinements, tables of structural data, and further magnetic susceptibility analysis.
- [31] R. D. Shannon, Revised Effective Ionic Radii and Systematic Studies of Interatomic Distances in Halides and Chalcogenides, Acta Crystallogr. **A32**, 751 (1976).

- [32] J. Wang, X. Y. Chong, R. Zhou, and J. Feng, Microstructure and thermal properties of RETaO_4 ($\text{RE} = \text{Nd, Eu, Gd, Dy, Er, Yb, Lu}$) as promising thermal barrier coating materials, *Scr. Mater.* **126**, 24 (2017).
- [33] V. Y. Markiv, N. M. Belyavina, M. V. Markiv, Y. Titov, A. M. Sych, A. N. Sokolov, A. A. Kapshuk, and M. S. Slobodyanyk, Peculiarities of polymorphic transformations in YbTaO_4 and crystal structure of its modifications, *J. Alloys Compd.* **346**, 263 (2002).
- [34] M. E. Fisher, Relation between the specific heat and susceptibility of an antiferromagnet, *Philos. Mag.* **7**, 1731 (1962).
- [35] G. A. Bain and J. F. Berry, Diamagnetic corrections and Pascal's constants, *J. Chem. Educ.* **85**, 532 (2008).
- [36] S. Mugiraneza and A. M. Hallas, Tutorial: a beginner's guide to interpreting magnetic susceptibility data with the Curie-Weiss law, *Commun. Phys.* **5**, 95 (2022).
- [37] S. T. Bramwell, M. N. Field, M. J. Harris, and I. P. Parkin, Bulk magnetization of the heavy rare earth titanate pyrochlores - A series of model frustrated magnets, *J. Phys. Condens. Matter* **12**, 483 (2000).
- [38] P. Mukherjee, Y. Wu, G. I. Lampronti, and S. E. Dutton, Magnetic properties of monoclinic lanthanide orthoborates, LnBO_3 , $\text{Ln} = \text{Gd, Tb, Dy, Ho, Er, Yb}$, *Mater. Res. Bull.* **98**, 173 (2018).
- [39] J. Rodríguez-Carvajal, Recent advances in magnetic structure determination by neutron powder diffraction, *Phys. B* **192**, 55 (1993).
- [40] N. D. Kelly, X. Liang, S. E. Dutton, K. Yamaura, and Y. Tsujimoto, High-pressure synthesis of the quantum magnet $M\text{-YbTaO}_4$ with a stretched diamond lattice (2025), under revision at *Phys. Rev. Mater.*
- [41] E. Solana-Madruga, C. Ritter, C. Aguilar-Maldonado, O. Mentré, J. P. Attfield, and A. M. Arévalo-López, $\text{Mn}_3\text{MnNb}_2\text{O}_9$: high-pressure triple perovskite with 1:2 B-site order and modulated spins, *Chem. Commun.* **57**, 8441 (2021).
- [42] T. R. Cao, H. Zhao, X. Huai, A. Quane, T. T. Tran, F. Ye, and G. Cao, Field-tailoring quantum materials via magneto-synthesis: metastable metallic and magnetically suppressed phases in a trimer iridate, *npj Quantum Mater.* 10.1038/s41535-026-00852-0 (2026).
- [43] Research data supporting this work will be made available at DOI:10.17863/CAM.125160.

Appendix A: PXRD Rietveld refinements

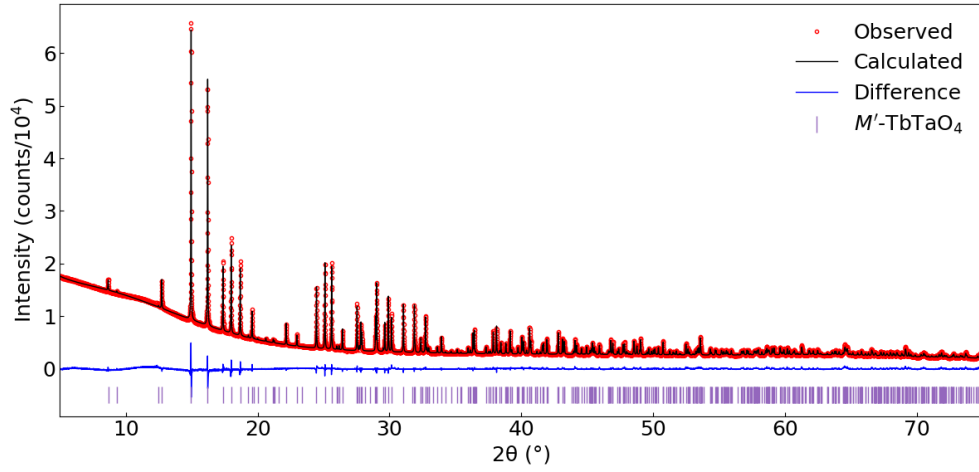


FIG. S1. Rietveld refinement against room-temperature synchrotron PXRD data ($\lambda = 0.82869 \text{ \AA}$) for M' -TbTaO₄. Red circles: observed data, black line: calculated pattern, blue line: difference pattern, purple tick marks: Bragg reflection positions.

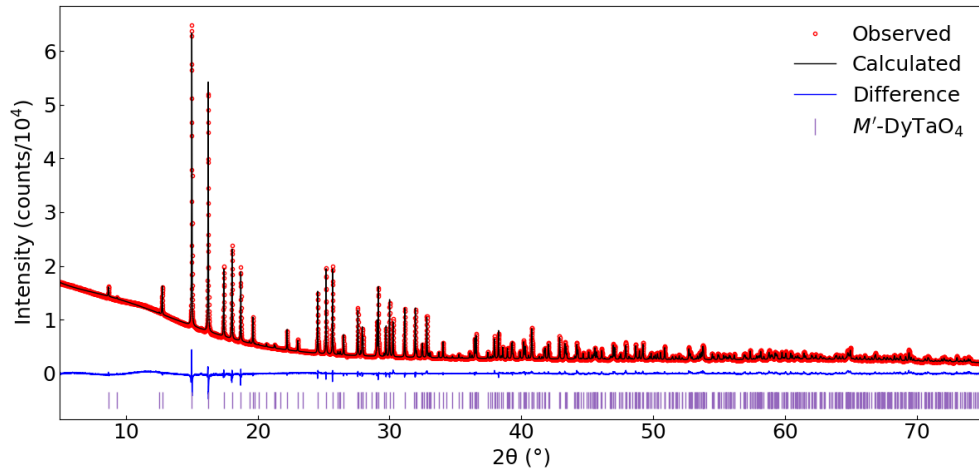


FIG. S2. Rietveld refinement against room-temperature synchrotron PXRD data ($\lambda = 0.82869 \text{ \AA}$) for M' -DyTaO₄. Red circles: observed data, black line: calculated pattern, blue line: difference pattern, purple tick marks: Bragg reflection positions.

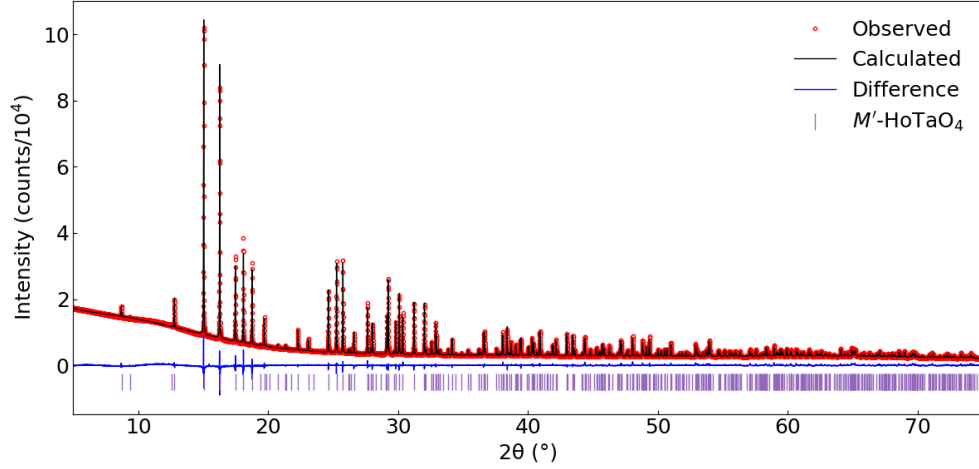


FIG. S3. Rietveld refinement against room-temperature synchrotron PXRD data ($\lambda = 0.82869 \text{ \AA}$) for M' -HoTaO₄. Red circles: observed data, black line: calculated pattern, blue line: difference pattern, purple tick marks: Bragg reflection positions.

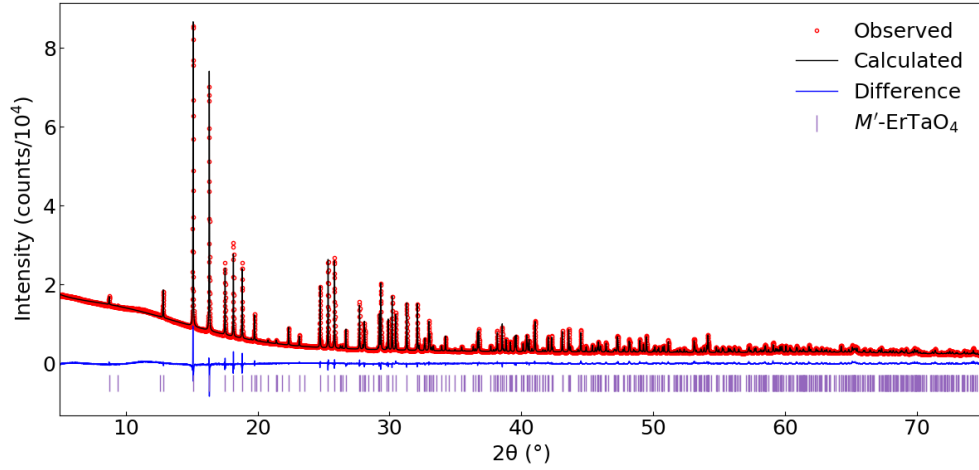


FIG. S4. Rietveld refinement against room-temperature synchrotron PXRD data ($\lambda = 0.82869 \text{ \AA}$) for M' -ErTaO₄. Red circles: observed data, black line: calculated pattern, blue line: difference pattern, purple tick marks: Bragg reflection positions.

Appendix B: Neutron refinements and structural parameters

TABLE S1. Refined structural data for M' -TbTaO₄ as a function of temperature, from TOF PND data. Space group: $P2/c$. Tb atom at (0, y_{Tb} , 0.25); Ta1 atom at (0.5, y_{Ta} , 0.75).

T (K)		1.5	30	100	300
a (Å)		5.13041(3)	5.13083(3)	5.13202(6)	5.14258(2)
b (Å)		5.48437(4)	5.48444(4)	5.48456(7)	5.49176(2)
c (Å)		5.33479(3)	5.33512(2)	5.33484(6)	5.33763(2)
β (°)		96.7799(4)	96.7771(5)	96.7594(9)	96.6566(3)
V (Å ³)		149.056(2)	149.080(2)	149.115(3)	149.728(1)
Tb1	y	0.73448(4)	0.73460(9)	0.73436(16)	0.73439(5)
Ta1	y	0.80844(7)	0.80833(9)	0.80851(17)	0.80767(6)
O1	x	0.74857(6)	0.74872(8)	0.74889(15)	0.74789(5)
	y	0.41258(6)	0.41269(8)	0.41278(14)	0.41318(5)
	z	0.39744(6)	0.39731(9)	0.39720(16)	0.39731(5)
O2	x	0.27061(6)	0.27056(9)	0.27050(16)	0.27091(6)
	y	0.06471(6)	0.06513(8)	0.06480(15)	0.06469(5)
	z	0.49557(6)	0.49579(9)	0.49596(16)	0.49543(6)
R_{wp} (%)		1.98	2.18	4.40	1.41
χ^2		2.33	4.37	1.48	3.19

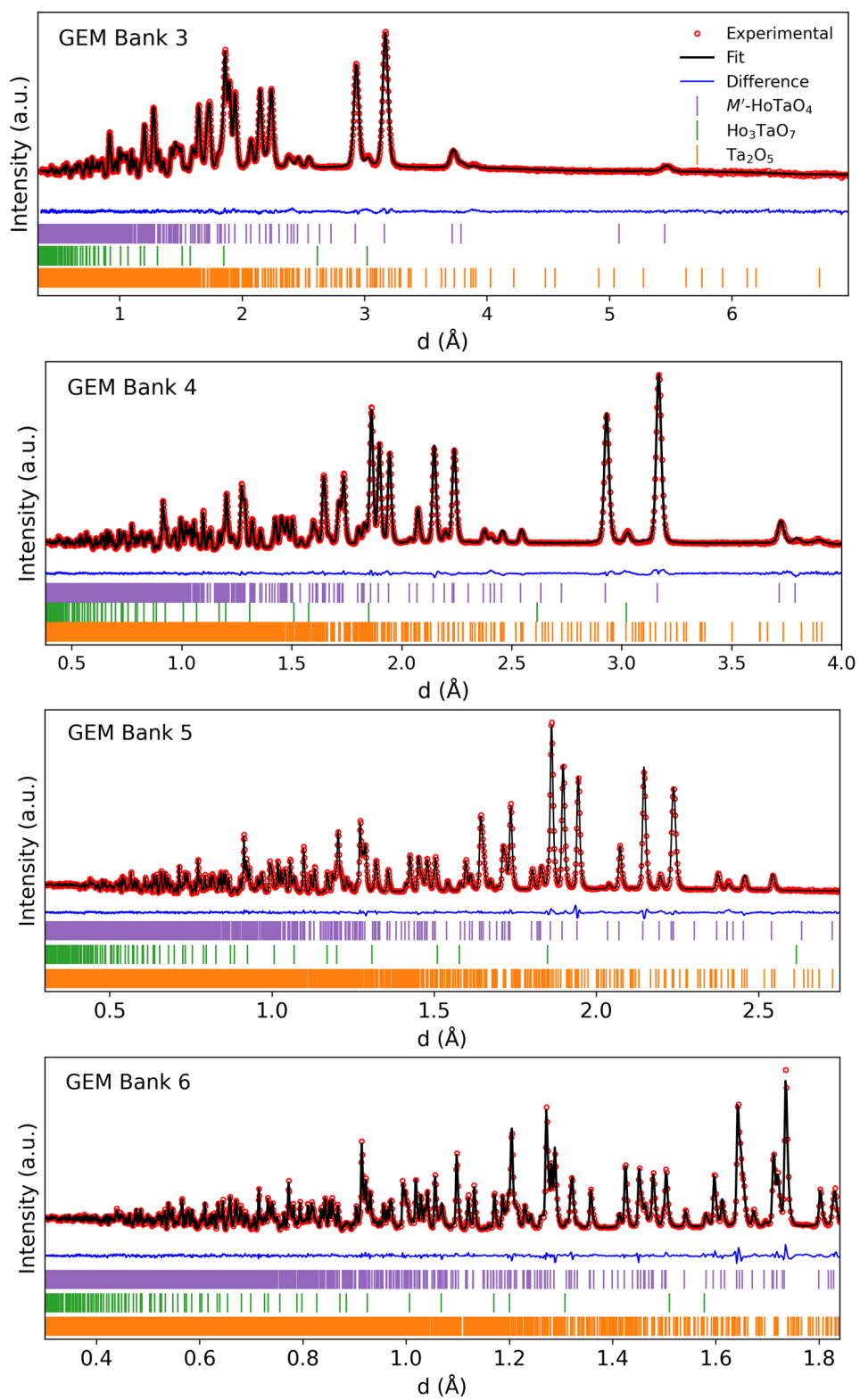


FIG. S5. Rietveld refinement against room-temperature TOF PND data for M' -HoTaO₄.

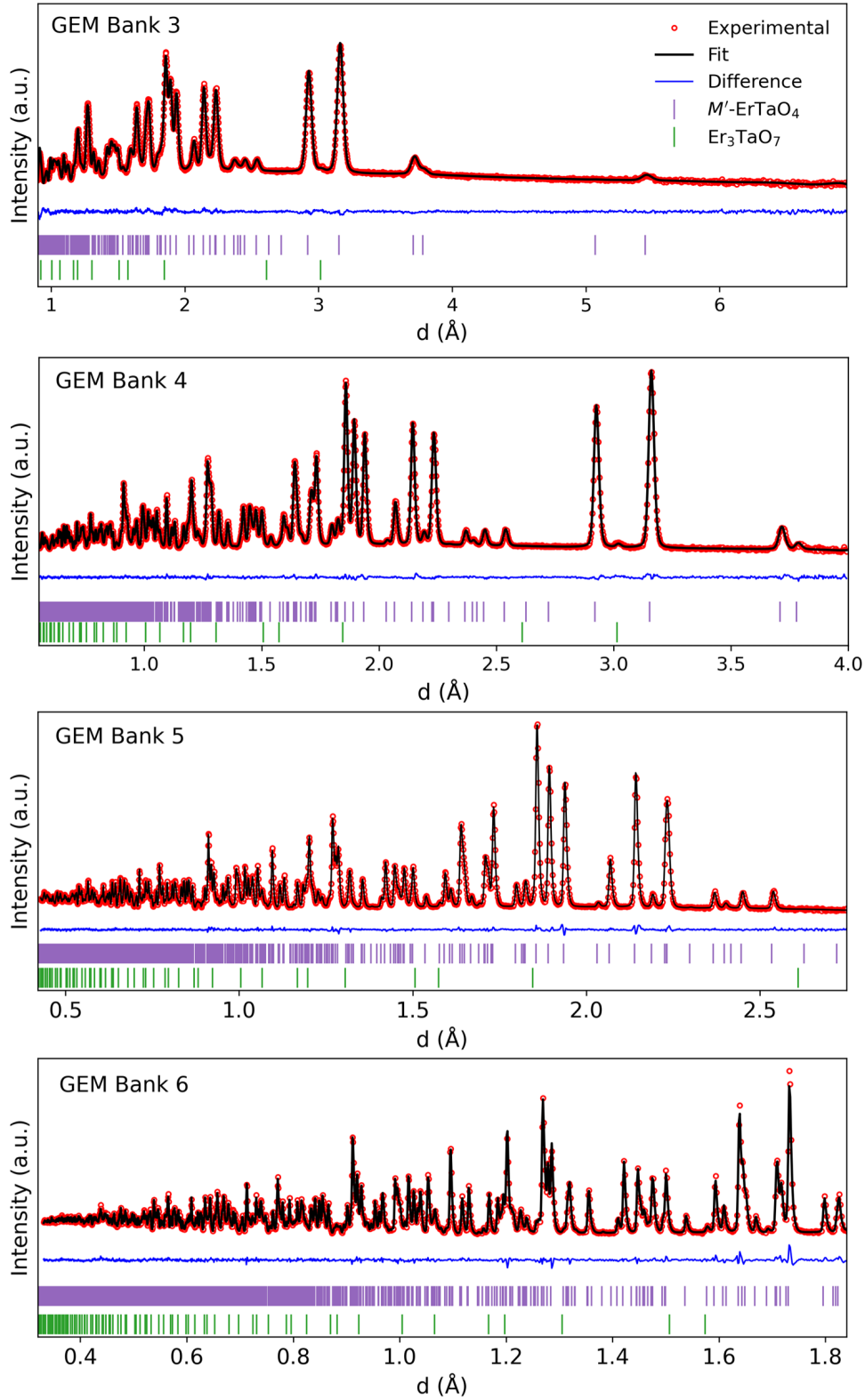


FIG. S6. Rietveld refinement against room-temperature TOF PND data for M' -ErTaO₄.

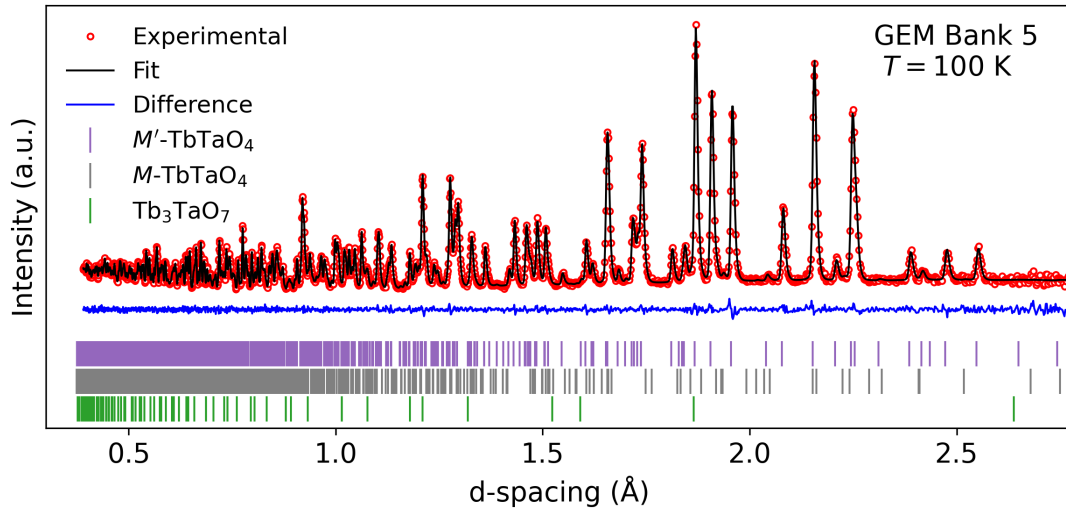


FIG. S7. Rietveld refinement against TOF PND data for M' -TbTaO₄ at 100 K.

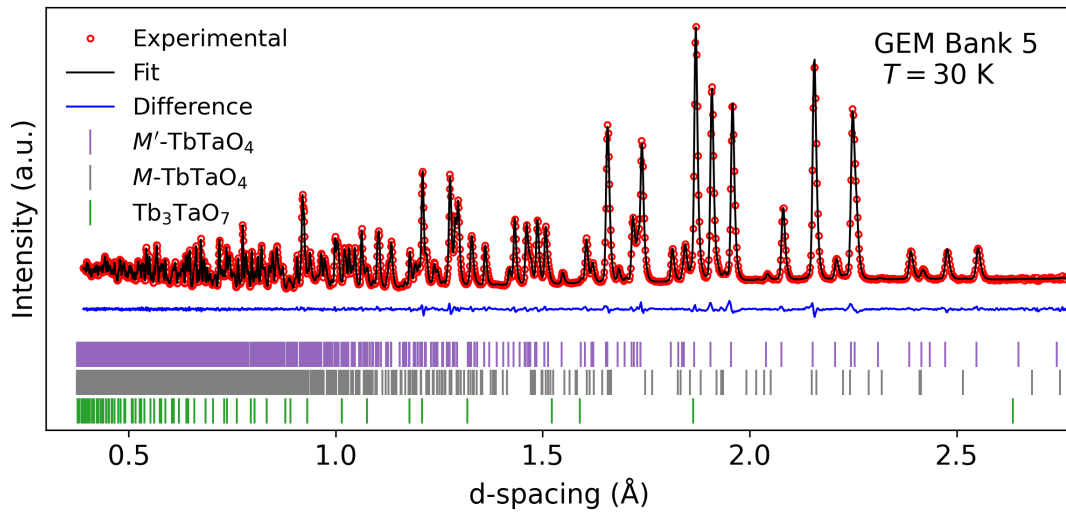


FIG. S8. Rietveld refinement against TOF PND data for M' -TbTaO₄ at 30 K.

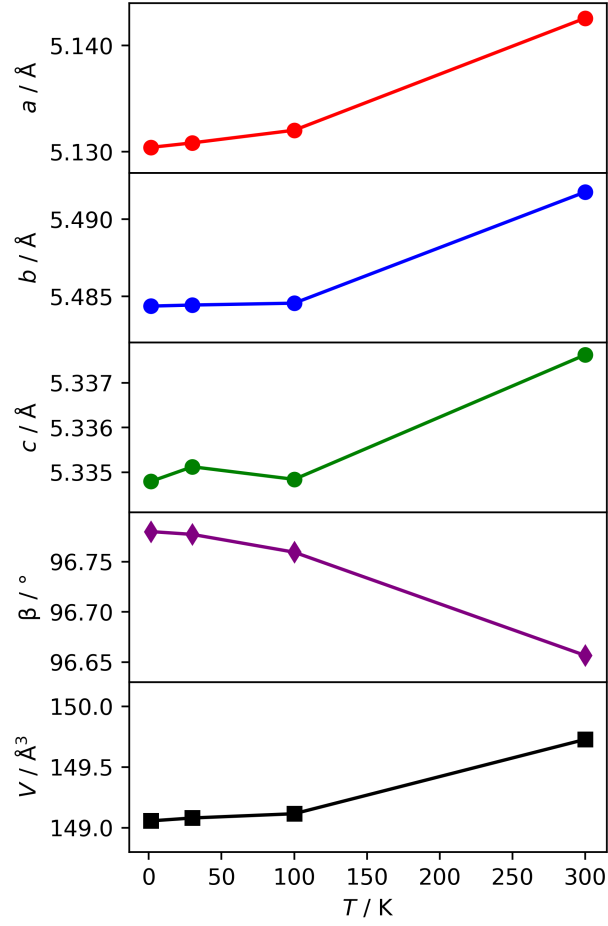


FIG. S9. Refined unit cell dimensions for M' -TbTaO₄ as a function of temperature, obtained by Rietveld refinement against TOF PND data. Error bars are smaller than the datapoints.

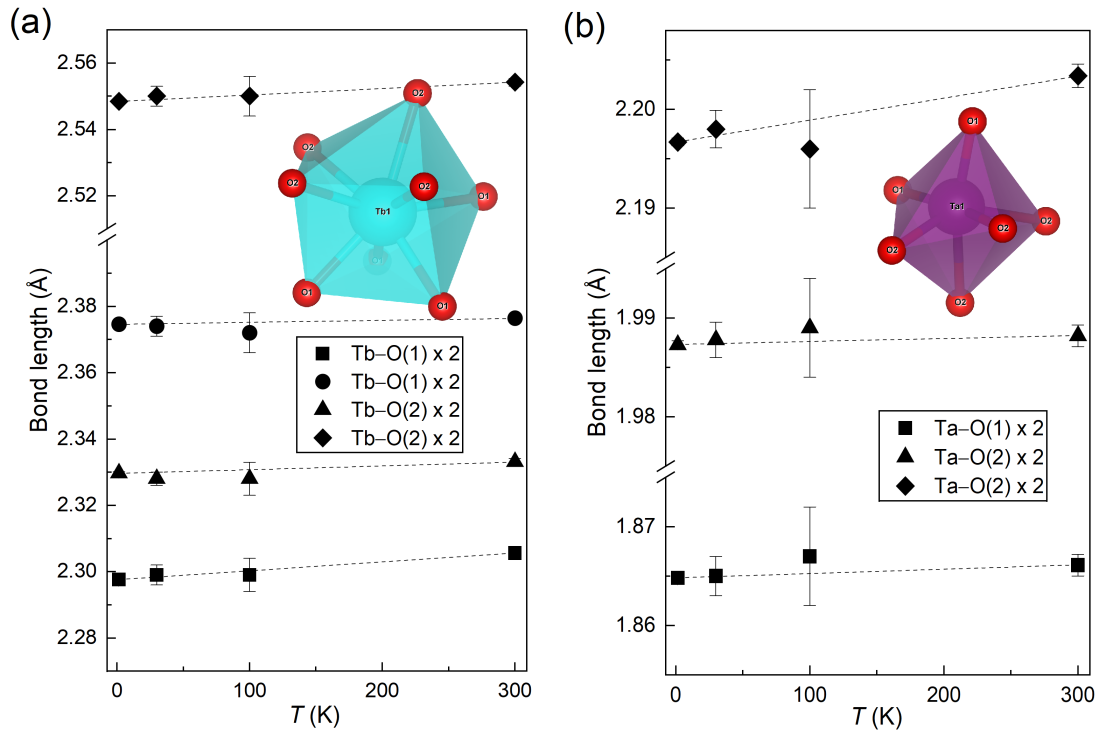


FIG. S10. Refined metal-oxygen bond distances for M' -TbTaO₄ as a function of temperature, obtained by Rietveld refinement against TOF PND data. Dashed lines are the lines of best fit.

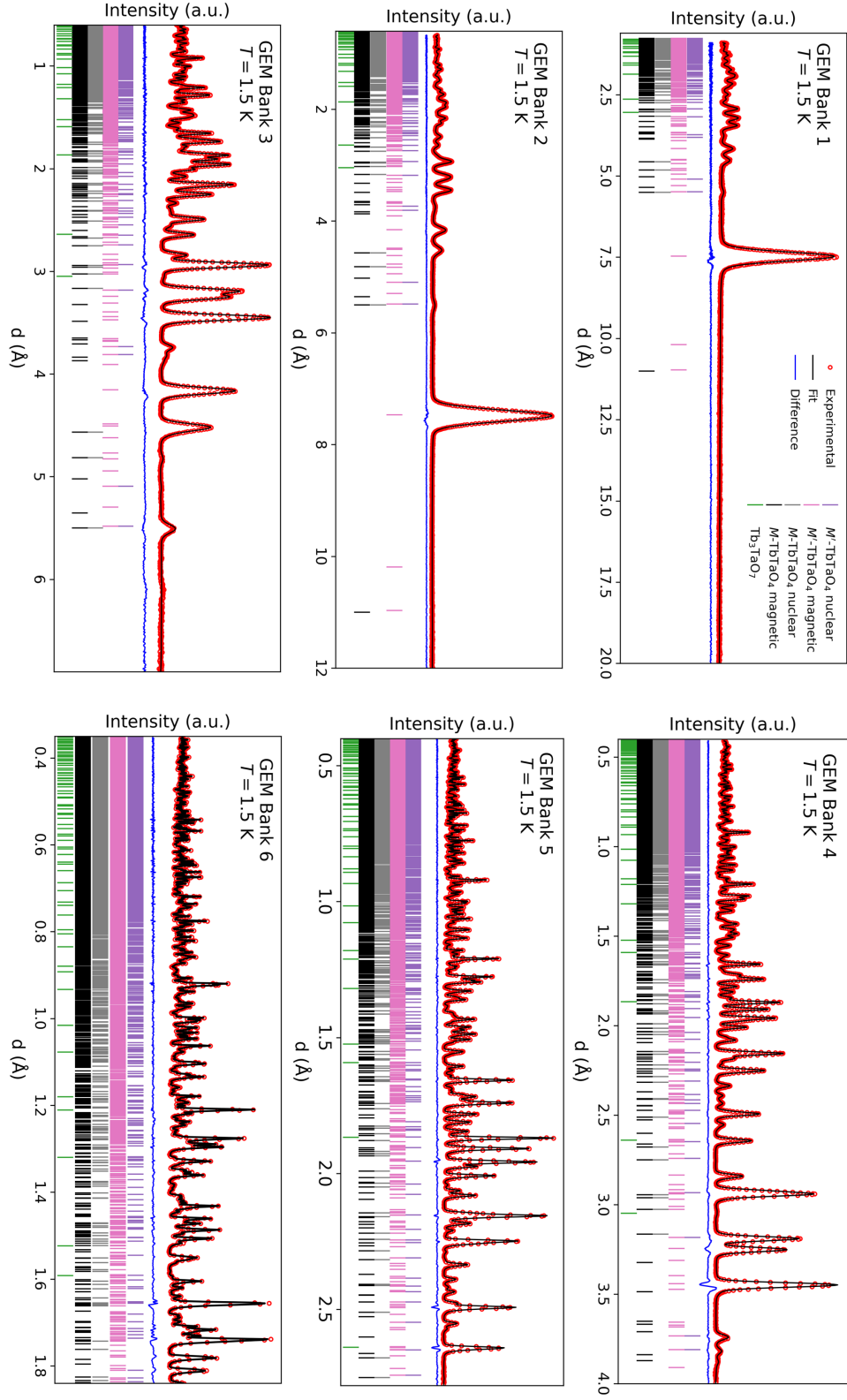


FIG. S11. Rietveld refinement against TOF PND data for M' -TbTaO₄ at 1.5 K, banks 1–6.

TABLE S2. Combined nuclear and magnetic structure model for M' -TbTaO₄ at 1.5 K, suitable for refinement in TOPAS using magnetic space group 14.80. To obtain the starting atomic positions for the combined model, the x and y fractional coordinates of the atoms in the nuclear unit cell were halved in order to account for the doubling of the cell in the a and b directions. Furthermore, two additional oxygen ions were required because of a difference in multiplicities of the Wyckoff sites. The pairs of atom sites O1/O3 and O2/O4 are each related by a translation of $(\frac{1}{2}, \frac{1}{2}, 0)$.

a (Å)	10.2616(13)			
b (Å)	10.9712(14)			
c (Å)	5.3358(7)			
β (°)	96.776(2)			
V (Å ³)	596.51(13)			
	x	y	z	B_{iso} (Å ²)
Tb1	0	0.36726(8)	0.25	0.017(4)
mlx, mly, mlz input (μ_{B} Å ⁻¹)	-0.0683(8)	0	1.5095(12)	-
Crystal Axes output (μ_{B})	-0.702(8)	0	8.053(6)	-
Cartesian Axes output (μ_{B})	-1.652(12)	0	7.997(6)	-
Ta1	0.25	0.40388(15)	0.75	0.081(5)
O1	0.37415(14)	0.20587(13)	0.3979(3)	0.240(3)
O2	0.13517(14)	0.03238(12)	0.4956(3)	0.240(3)
O3	0.87415(14)	0.70587(13)	0.3979(3)	0.240(3)
O4	0.63517(14)	0.53238(12)	0.4956(3)	0.240(3)
R_{wp} (%)	1.98			
χ^2	2.33			

Appendix C: Additional susceptibility data

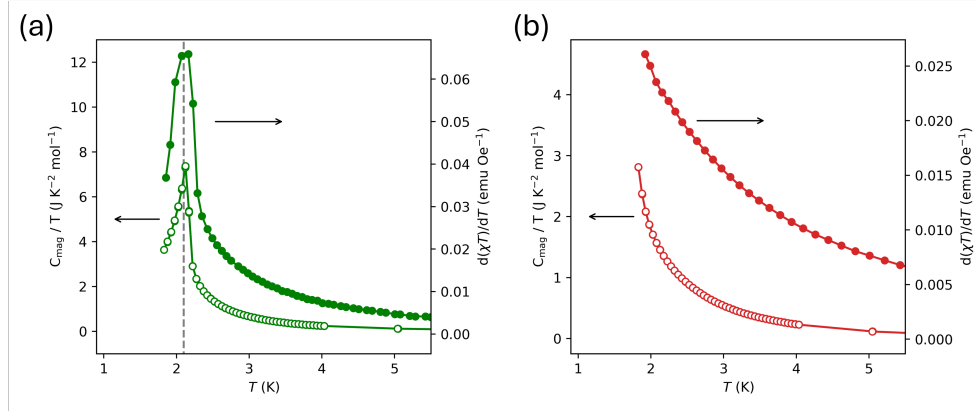


FIG. S12. (a) Comparison of the heat capacity data with the derivative of the susceptibility, $d(\chi T)/dT$, for M' -TbTaO₄. The peaks in the two plots occur at the same temperature, marked with a grey dashed line, consistent with expected behaviour for a long-range ordered antiferromagnet [34]. (b) Heat capacity data and $d(\chi T)/dT$ for M' -DyTaO₄. There is no peak in either the heat capacity or $d(\chi T)/dT$.

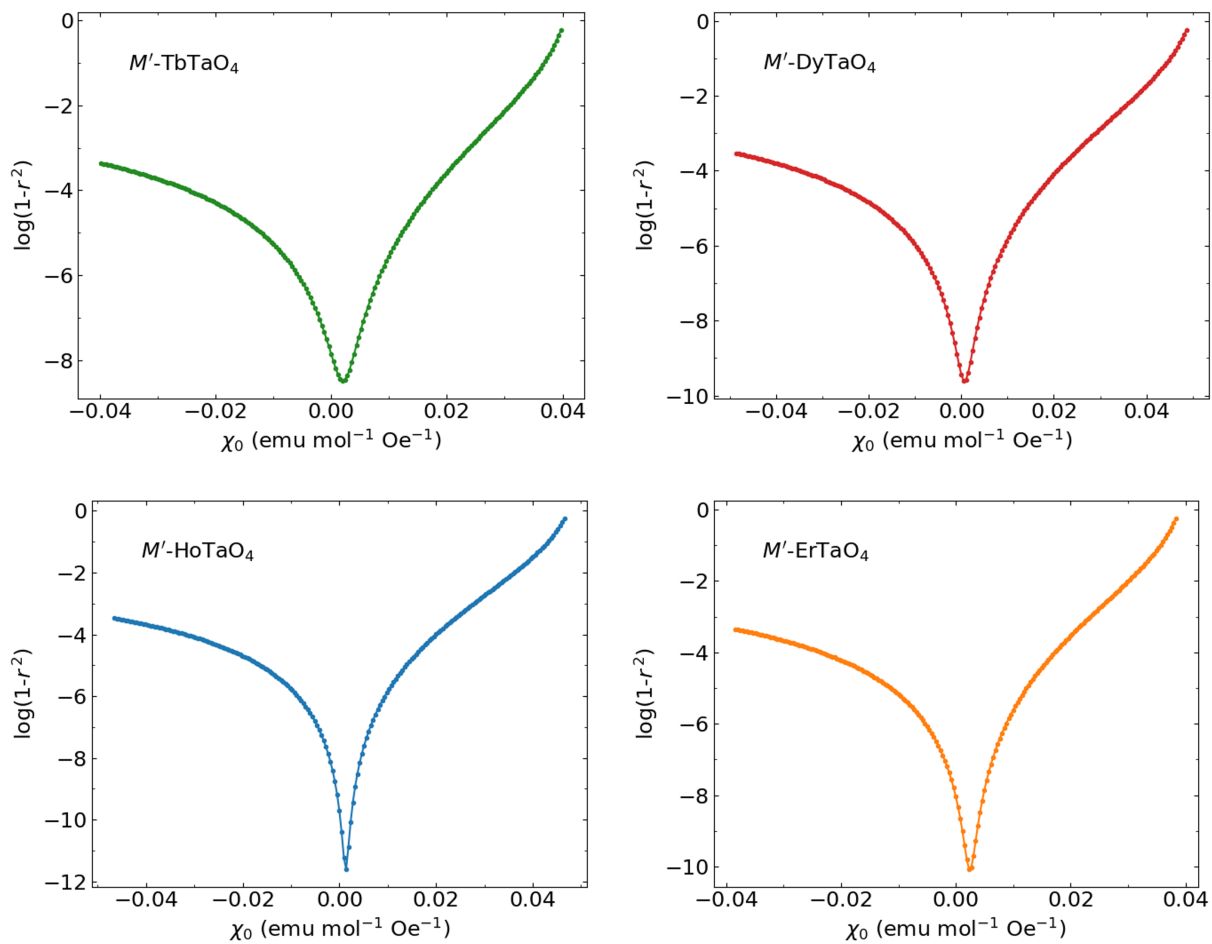


FIG. S13. Optimisation of the fixed susceptibility contribution χ_0 for the four M' - Ln TaO₄ compounds in this study.